Chapter

Integrated Manufacturing of Fine-Grained Stainless Steels for Industries and Medicals

Tatsuhiko Aizawa, Tomomi Shiratori and Takafumi Komatsu

Abstract

Austenitic stainless steels have been widely utilized in industries, infrastructures, housing structures, kitchen components, and medical tools. Higher hardness and strength as well as more improvement of wear and corrosion toughness are often required in the industrial and medical applications. Fine-grained stainless steel (FGSS) provides a solution to increase the strength without loss of ductility and toughness. Deeper research and development in manufacturing of FGSS is required to make full use of its properties toward its applications in industries and medicals. First, its mechanical properties and microstructure is introduced as a basic knowledge of FGSS with comparison to the normal stainless steels. Mechanical and laser machinability of FGSS is stated and discussed to finish the products in seconds. Its performance in metal forming and diffusion bonding is explained to explore its applications in third. Its surface treatment and tooling is discussed to describe the grain-size effect on the low temperature plasma nitriding and to demonstrate its effectiveness in die-making in forth. Finally, every aspect in manufacturing of FGSS sheets and solids is summarized as a conclusion.

Keywords: stainless steels, fine grain, milling, laser machining, metal forming, diffusion bonding, surface treatment, tooling, medical applications

1. Introduction

Hall-Petch relationship was found in 1951 [1] and 1953 [2]. Since this finding, the grain-size refinement has become one of the key development topics to improve properties of metals and alloys. High-pressure torsion (HPT) is one of the early technologies to refine microstructure for aluminum or copper [3]. A disk of these material is confined in a cylinder and subjected to torsion by rotating punch under high vertical pressure. As the strains increased during torsions in a disk, the grain size of these materials becomes smaller; then rounding by four times increases its hardness together with homogeneity of grain size [4]. However, the method is only applicable for relatively soft metallic alloys. It is difficult to apply to hard metals such as carbon steels or stainless steels. In addition, since the strains during a torsion is different in the radial direction of disk, the grain size remains larger than that in outer diameter; the rotation is not enough. Hence, this method might be suitable to create hard surface around the edge of products like a miller disk in the office copy machine; its application to bulk work materials is limited by cost

and production process. The continuous production process, like rolling, stamping, or cutting by lathe in the production area, need proper and stable bulk materials. For the part productions of medical, IT, or automobile industries, stable shapes of bulk material are important to produce precise parts with high accuracy and lower cost. Especially, minimally invasive medical treatment needs smaller devices and higher strength. Thus, wire and coil shapes are preferable for these parts industries. Often, the improvements of material need changing the chemical composition, but it usually needs approval from medical regulations in each country. The approval waist a lot of investments and time. Thus, the technology of improvement without changing the chemical composition was evitable. Fine-grained stainless steel (FGSS) is highlighted as the most reliable work materials to fabricate the miniature automotive parts as well as the fine medical components.

In the present chapter, various manufacturing methods are employed to investigate each workability of FGSS materials; e.g., mechanical and lase machining, metal forming, diffusion bonding, and surface treatment after explanation on their mechanical properties and microstructure. The superiority of FGSS to this integrated manufacturing is a key to utilize FGSS to fabricate the miniature mechanical parts and medical fine components.

2. Mechanical properties and microstructure of FGSS

There are only two ways to produce FGSS in the production place in 2019. One method is oval-square rolling, which has been developing by Torizuka and Muramatsu since 1998 as a suitable means to produce the bar and wire [5]. **Figure 1** shows the change of work cross section during oval-square rolling process. Steel or stainless steel coil with ϕ6.0 mm is used as a starting work material. Grains are decreased by heating and severe plastic deformation with use of oval and square shaping rolls. The high strains at the center of coil drive dynamic recrystallization from 20 to less than 3 μm across the all cross section. This process continues till coil diameter reaches ϕ3.0 mm.

Figure 2 compares the IPF (inverse pole figure) of AISI316L by Electron Back Scattered Diffraction Pattern (EBSD) before and after this oval-square rolling. There are wide range of grain size before the process and these are austenite (**Figure 2(A)**), then the average grain size becomes 1.3 μm (**Figure 2(B)**).

The tensile strength of initial work ranges from 520 to 580 MPa. This is increased up to 980–1150 MPa by the grain reduction by 1/10 just after the Hole-Petch relationship. To be noticed, this strengthening also accompanies with work hardening and processing-induced transformation to martensite. This difference in strengthening mechanism between work hardening and grain-size reduction must be distinguished carefully.

Inverse phase transformation method is also cost effective method to produce the thin FGSS sheets [6, 7]. The grain-size reduction is driven by the inverse phase transformation from martensite by work hardening to austenite phase. Austenitic stainless steels of type AISI304 were employed as a work. The work materials were manufactured in a heat batch processing. **Table 1** shows the chemical composition of the material.

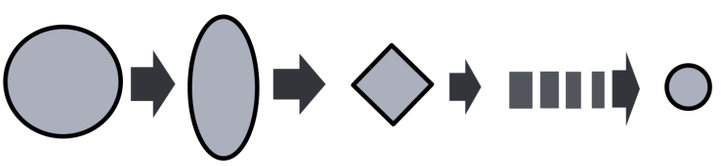

Figure 1.
Illustration on the wire fabrication by the oval-square rolling process.

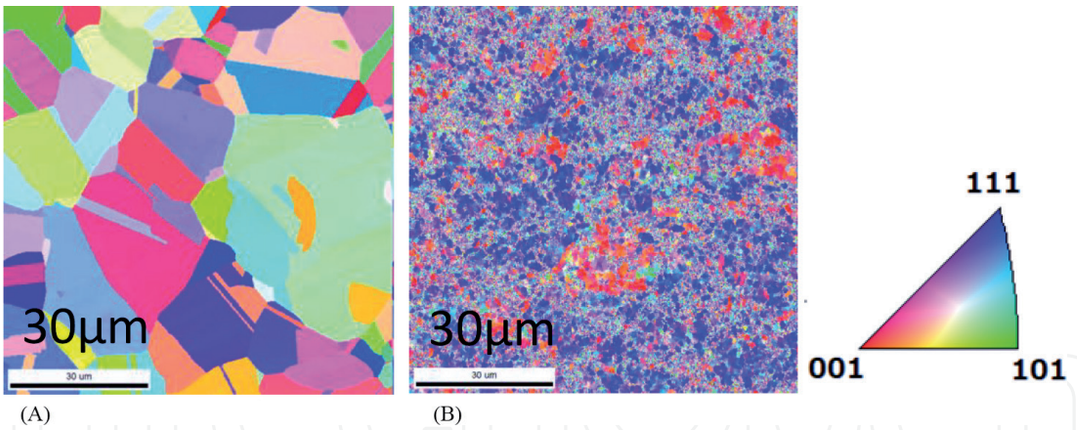

Figure 2.
Picture of grain condition by EBSD. (A) Left: before oval-square rolling. The average grain size is 14.7 μm and (B) right: after the process. It becomes 1.3 μm.

	Composition %
Carbon (C)	0.06
Silicone (Si)	0.4
Manganese (Mn)	1.09
Phosphorus (P)	0.03
Sulfur (S)	0.004
Nickel (Ni)	8.03
Chromium (Cr)	18.02

Table 1.
Chemical composition of the specimen.

The normal grain stainless steel was formed to reduce the plate thickness from 3 to 0.2 mm in rolling with heat treatment. **Figure 3(A)** shows the microstructure, which is observed by EBSD. θ is the crystal orientation angle; and α' and γ are the crystal phase. The marten-sites structures are observed and the grain sizes are ranged from 2 to 20 μm, where the average grain size is 9.10 μm.

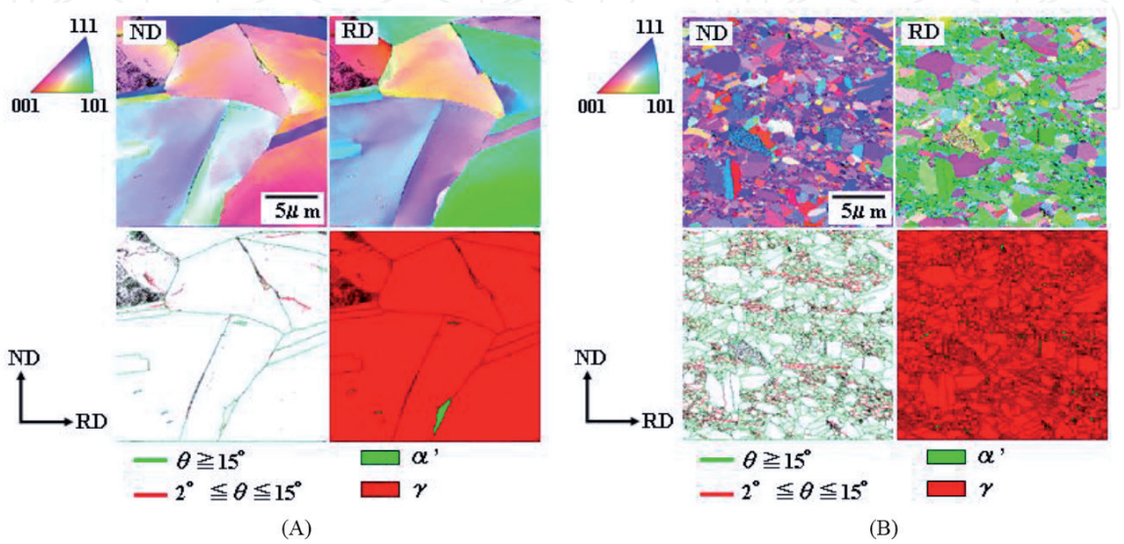

Figure 3.
Picture of grain condition by EBSD. (A) Left: normal grain stainless steel. The average grain size is 9.8 μm and (B) right: FGSS by reverse phase transformation. The average grain size is 1.52 μm.

		Normal grain steel	Ultra fine-grained steel
Vickers Hardness [HV]		260	260
Tensile strength [MPa]	RD	870	919
	ND	858	880
Elongation [%]	RD	51.1	42.5
	ND	57.5	46.4
Ave. grain size [μm]		9.10	1.52

Table 2.
Mechanical properties.

The fine-grained stainless steel was formed with repeating plastic deformation and reverse phase transformation. **Figure 3(B)** shows the microstructure, where the average grain size is 1.52 μm.

Although the grain size was different among specimens, their ultimate tensile strength became around 900 MPa, irrespective of the grain size.

Table 2 shows the mechanical properties of the normal stainless steel and FGSS. Here, the mechanical properties are similar to each other. The hardness and tensile strength is controlled by work handing for normal grain, and by decreasing the grain size by reverse phase transportation for FGSS. These different hardening methods for stainless steel should be distinguished in terms of microprocessing.

As a summary, FGSS has refined microstructure with the average grain size of 1.5 μm and higher ultimate strength than 900 MPa. Its hardening process is governed by the reverse phase transformation in different from the work hardening in the normally grained AISI304.

3. Mechanical machining of FGSS

Several researchers have discussed the effect of grain size and boundaries in micro/nano processing such as cutting, piercing, forming, and so on. As the removal depth becomes smaller than the grain size, which is usually more than 20 μm, it is difficult to ignore the crystalline direction, size, and distributions in such microprocessing.

Simoneau et al. discussed the grain-boundary effect in medium carbon steels, and he found the different grain deformations in cutting chips [8]. Lee et al. discussed material-induced vibration, which is caused by the changing crystallography of the material substrate [9, 10]. They also analyzed the variation in microcutting forces in diamond tool turnings of crystalline materials, based on a microplasticity model and spectrum analysis technique [11]. Furukawa and Moronuki discussed the grain-boundary effect during the cutting of large grained steel. They found that when the grain boundary is crossed by the tool, the cutting force increases [12]. Komatsu have also discussed the effects of grain size on two-dimensional microcutting [13–15]. When the grain size is less than 3 μm, the cutting tool vibration is reduced, and the quality of the groove is improved. This is because small grained materials are regarded as homogeneous materials in terms of hardness.

However, study of the effect of grain size on other processes and product functions, based on materials of various grain sizes, are limited because the size of bulk material with FGSS has been too small for the studies.

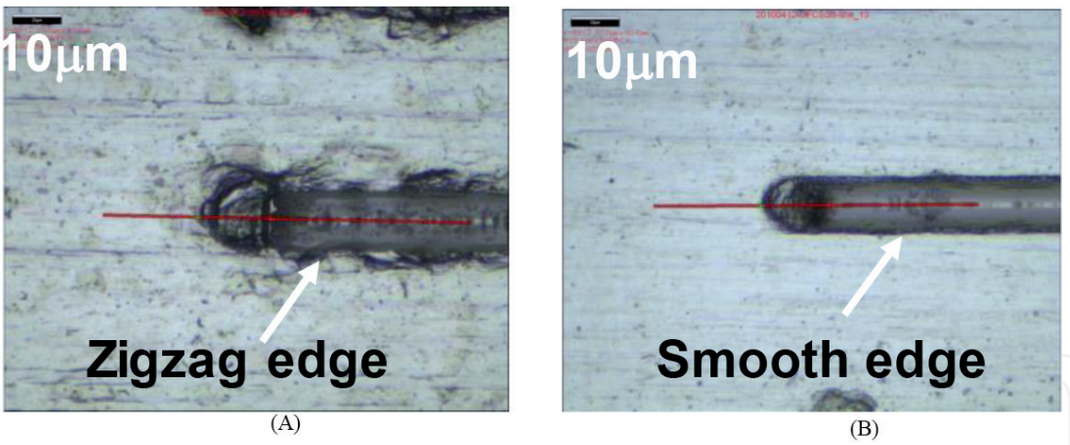

Figure 4.
Picture after microcutting by diamond tool. (A) Left: groove condition on normal grain stainless steel. The average grain size is 9.8 μm and (B) right: Groove condition on FGSS by reverse phase transformation. The average grain size is 1.52 μm. FGSS can get smooth edge when cutting in microscale.

This chapter will present the cutting process of FGSS. Two different grain sizes were employed, as is mentioned before, to discuss the effect of the grain size on the cutting process in the microscale.

Figure 4 shows the surface finishes by diamond tool in microcutting. The groove width and depth was about 8 μm. It should be noted that the edge quality is incredibly improved as compared between **Figure 4(A)** and **(B)**. This feature had benefits for fine parts or medical equipment.

The effect of the grain size was discussed with measuring the cutting forces and their oscillation. The stability in the cutting process was associated with the oscillation of the cutting force in **Figure 5**.

When large grain material was cut, the tool was widely vibrated as shown in **Figure 5(A)**, because the deformation reached to the grain boundaries and it needed force more. On the other hand, smaller grain had narrow length of between grain boundaries, it constantly effected on the cutting force [13, 14] in **Figure 5(B)**. Komatsu discovered some more features in microcutting this FGSS. Higher shear-plane angles, cutting FGSS less than 5 μm, reduce the cutting force even the tensile strength is increased [12]. This features reduced the burr. Ball end-mill cutting examined for these material and the burr size become from 1/5 to 1/3 [15]. Finally, the residual strains were also reduced by using FGSS.

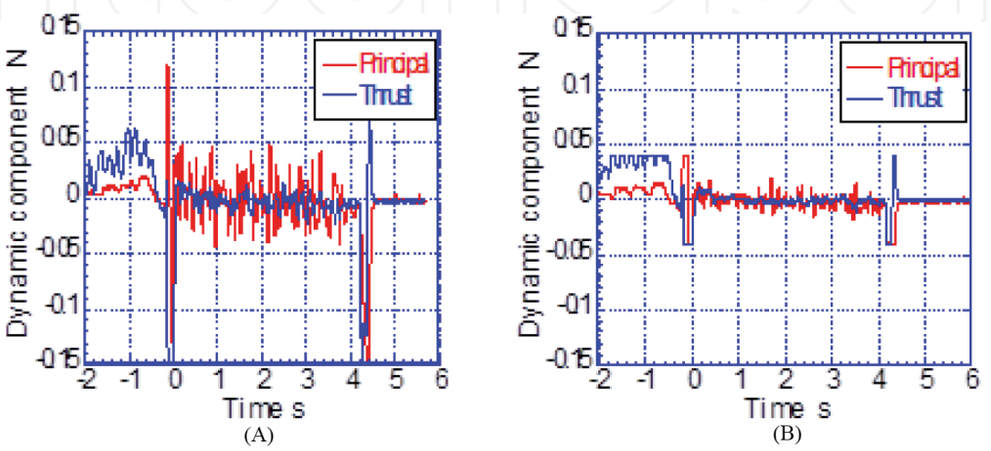

Figure 5.
Differentials of vibration results from principal and thrust cutting force. (A) Left: the average grain size is 9.8 μm and (B) right: the average grain size is 1.52 μm.

In summary, mechanical machinability of FGSS is much improved by fine-grained microstructure; smooth cutting edges, reduction of in situ vibrations and burr size.

4. Laser machining of FGSS

Laser machining grew up as one of useful means to produce miniature parts. This laser processing has two different aspects; one is thermal process like welding, and the other is mechanical process. When producing accurate parts for medical or precision parts, thermal effects on the works surface became a main driving force in the CO_2-laser machining. When the laser wave length became shorter or when using the pico- or femtosecond laser, the thermal effects are ignored because materials are removed before transferring the temperature [16]. Siegelet et al. investigated the picosecond pulse ablation behavior and industrial relevance in 2009. He noted that the accurate surface and structures were introduced and the thermal effect was ignorable [17].

Since the picosecond laser reduces the thermal influence on cutting, the grain-size effect on the laser machining changes by its mechanical process. Using FGSS is one of the methods to apply to the enhanced parts of medical, because it has higher tensile strength and hardness without changing any chemical composition. Komatsu used the picosecond laser to investigate the grain-size effect on the laser machining of AISI 304 with the thickness of 1.5 mm [18]. **Figure 6(A)–(C)** shows the cross-sectional images after laser drilling AISI304 sheet with different grain sizes by 30 times. The laser machining system (PANASONIC AP-3220) was employed; the laser output was 500 mW, the wavelength, 1053 nm, the pulse duration, 15–25 ps, and the repetitive frequency, 5 kHz. The spot size was constant by 30 μm.

There are significant differences of processing depth in different grain size. When processing smaller grains such as FGSS (1 or 2 μm), the depth of groove was from 0.1 to 0.12 mm. On the other hand, there are from 20 to 40% deeper groove in large grain's material. After 30 times laser processing, the material nearly cut. **Figure 7** describes the relationship between the one-shot machined depth and the grain size. Deeper groove is formed by machining the large grain AISI304, while shallower groove becomes unstable in case of FGSS. This might come not only from the hardness of material but also from the absorptivity, which related to surface roughness and structure [18]. The smaller grain size is preferable to micro deep laser cutting.

In summary, laser machinability of FGSS is characterized by precise cutting of relatively shallow microgrooves.

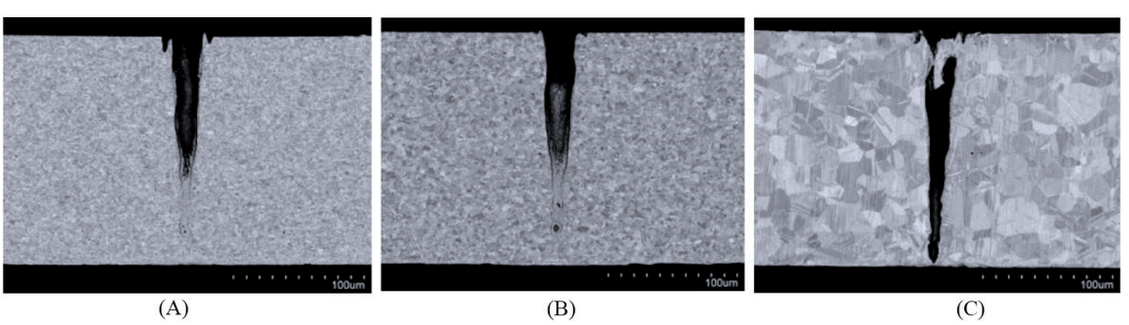

Figure 6.
SEM cross-sectional image after laser processing machining the AISI304 with different grain size (d) by 30 times in the same condition. (A) Left: D = 1.1 μm, (B) center: D = 2.0 μm, and (C) right: D = 9.2 μm.

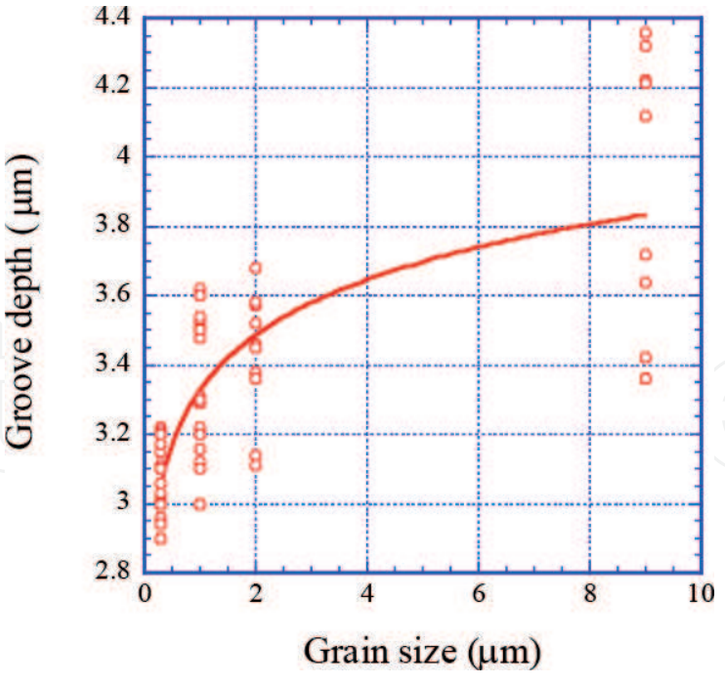

Figure 7.
Relationship between the grain size and groove depth after one-shot laser processing.

5. Metal forming of FGSS

5.1 Deformation and transformation in micropunching of FGSS304

As well known, size effects were observed during metal forming [19–21]. The size effect also occurs in punching process. In this chapter, introducing the difference in deformation and transformation of austenitic stainless steel AISI304 when micropunching with grain size changing. AISI304 stainless steel causes strain-induced transformation during plasticity process [22]. The strain-induced transformation of AISI304 austenitic stainless steel was classified as non-diffusive shear transformation, and transformation occurs in grain-size units [23]. Therefore, shear deformation in micropunching became complicate.

5.2 The stability of sheared surface length when changing a grain size

Figure 8 shows four IPFs of AISI304 stainless steels with different grain sizes, which were analyzed by EBSD [24]. Grain size (Gs) 7.5 μm was standard grain size of AISI304. The grain size from Gs 3.0 to Gs 1.0 μm were specially minimized AISI304 that were not changed chemical composition. The characteristics of materials were shown in **Table 3** [24]. From this table, as grain size decreasing, 0.2 % proof stress and tensile strength increasing and elongation became decreasing. The Hall-Petch relationship works effectively in these grain-size conditions.

Figure 9 shows the constitution of sheared surface and cross-sectional SEM images of punched microhole [24]. The punching condition was following; material thickness 100 μm, punch diameter 80 μm, die diameter 87 μm, clearance between punch and die 3.5 μm, punching speed 4.2 mm/s. The sheared surfaces were consisted by shear droop, burnished surface, and fractured surface, respectively. The burrs were not shown in this figure. **Figure 10** shows the ratio of sheared surface that calculated from five samples [24]. From this figure, as grain size decreasing, the shear droop ratio became small and fractured surface ratio became large. However,

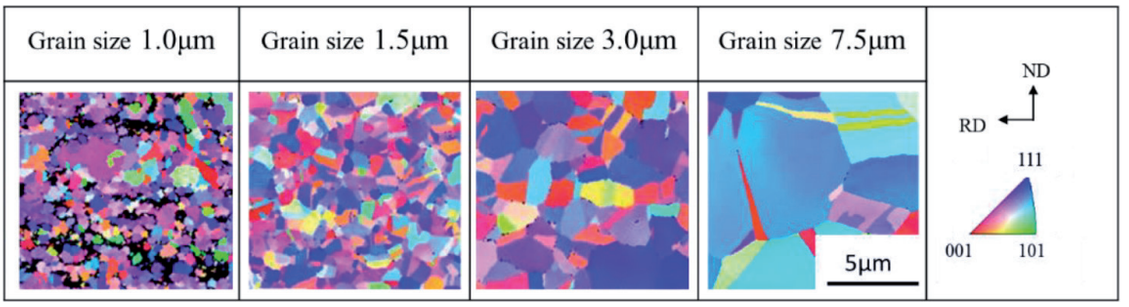

Figure 8.
EBSD inverse pole figure of four grain size austenitic stainless steel AISI304 including FGSS304.

Grain size [μm]	**1.0**	**1.5**	**3.0**	**7.5**
Tensile strength [N/mm^2]	1181	875	845	803
0.2% proof stress [N/mm^2]	1000	599	504	433
Elongation [%]	6.0	45.8	49.5	56.6
Hardening exponent [−]	—	0.31	0.37	0.43
Vickers hardness [HV]	350	261	227	191

Table 3.
Mechanical characteristics of four grain size austenitic stainless steel AISI304 including FGSS304.

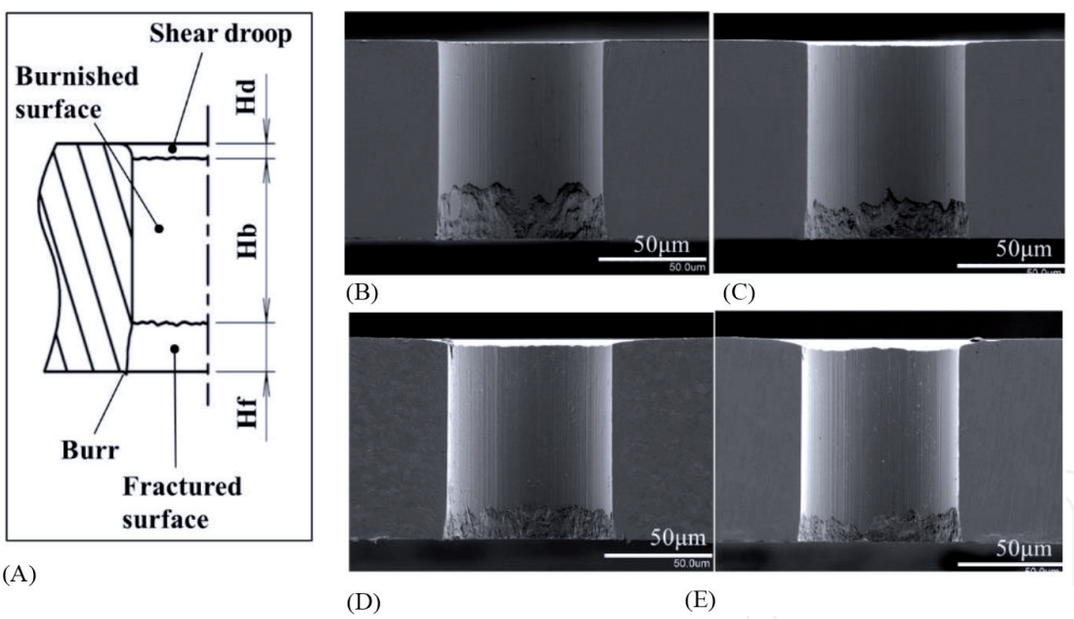

Figure 9.
Constitution of sheared surface and SEM images of cross section of micropunched hole. (A) Constitution of sheared surface, (B) Grain size 1.0μm, (C) Grain size 1.5μm, (D) Grain size 3.0μm, (E) Grain size 7.5μm.

from **Figure 11**, the standard deviation of burnished surface ratio took a different trend [24]. The grain size 3.0 μm took a smallest standard deviation. It was found that the stability of the sheared surface length changing with grain size.

5.3 Process affected zone in micropunched hole

Why the stability of burnished surface length changed with grain size? **Figure 12** shows the EBSD analysis results of punched samples with three different varying grain sizes of 1.5, 3.0, and 7.5 μm, respectively. The punching conditions were following; the material thickness is 100 μm, the punch diameter, 80 μm, the die diameter, 85 μm,

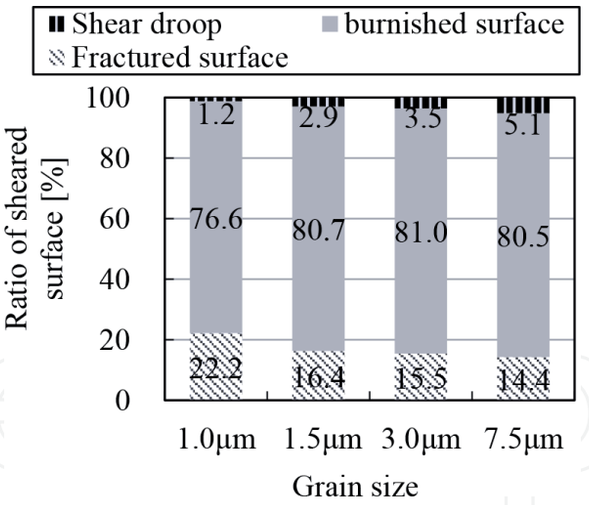

Figure 10.
Ratio of the sheared surface.

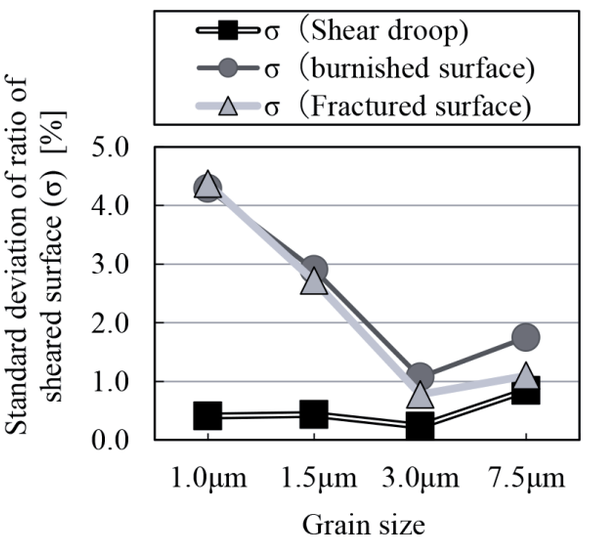

Figure 11.
Standard deviation of ratio of sheared surface.

the clearance between punch and die, 2.5 μm, and the punching speed, 4.2 mm/s. In **Figure 12**, IQ + phase map shows the grain phase and the IQ + KAM (Kernel average misorientation) map shows the grain misorientation angle. The grain misorientation angle was known to correspond to equivalent plastic strain [25].

From **Figure 12(A)–(C)**, the strain-induced martensitic α' phase was remained along with the punched hole. From the grain size 7.5 μm phase map results (**Figure 12(C)**), the border line between α' phase and austenitic γ phase looks like hackly. This trend is caused by grain unit transformation. On the other hand, from the grain size 1.5 μm phase map results (**Figure 12(A)**), the border line between α' phase and γ phase looks like stable. From the **Figure 12(D)–(F)**, process-affected areas were existed along with punched hole, respectively. Especially, the highly 5° misorientation angle color red has spread along with the wall of punched hole at each samples.

5.4 Deformation and transformation mechanism in micropunching of FGSS304

Figure 13 shows the total frequency of α'-phase and total amount of misorientation angle that calculated from the sample shown in **Figure 12** and the other two samples. From **Figure 13(A)**, Z minimizes at the grain size of 3 μm. From **Figure 13(B)**,

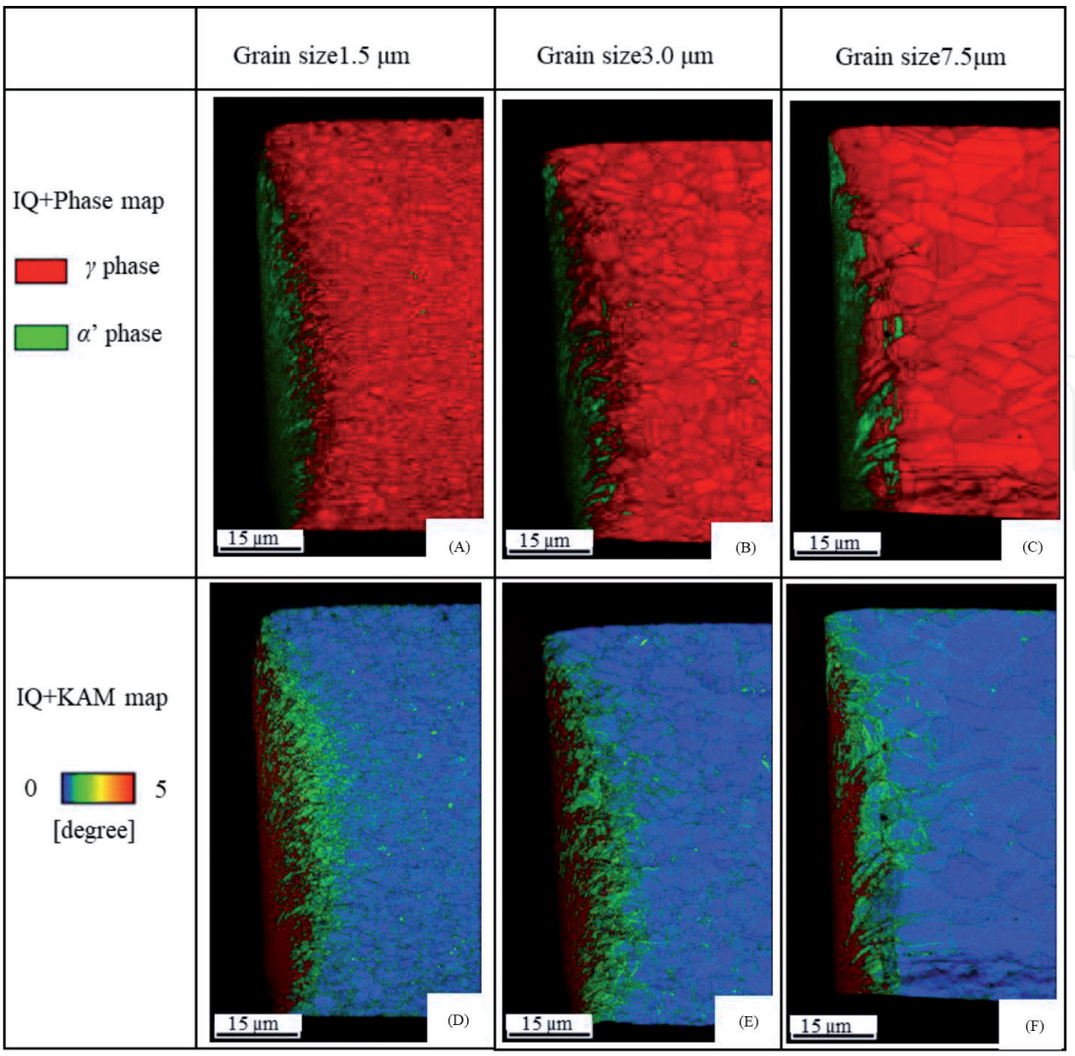

Figure 12.
EBSD analysis results of cross section of punched hole.

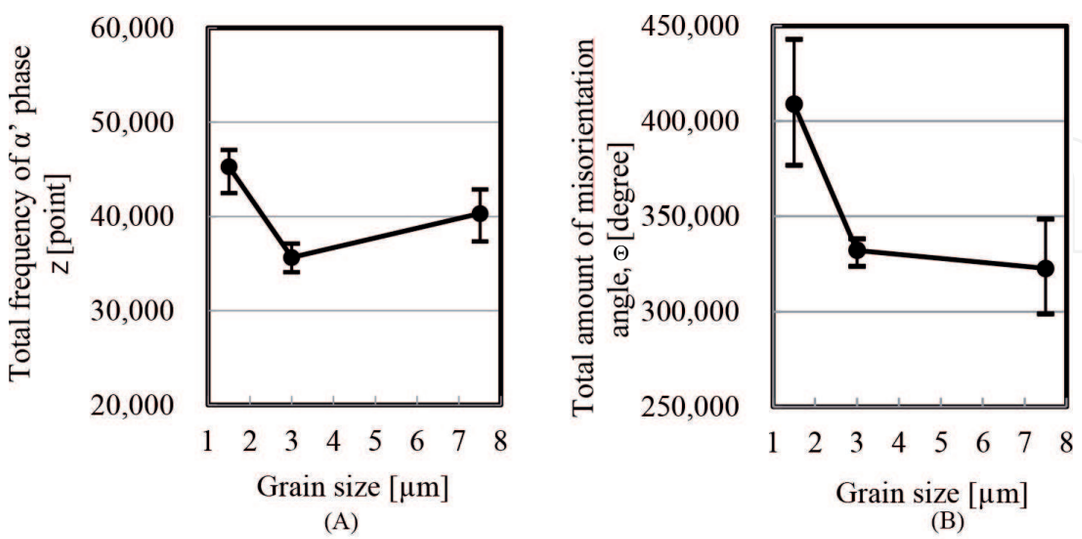

Figure 13.
Total frequency of α′-phase and total amount of misorientation angle in the cross section of punched hole. (A) Total frequency of α′ phase and (B) total amount of misorientation angle.

Θ maximizes at the grain size of 1.5 μm; Θ1.5 μm is more than Θ3.0 μm by 24 %. When choosing the grain size 1.5 μm, small grain size has limited work hardening ability. So that, strain-induced transformation works actively and the frequency of

α' phase more increase than the other large grains as shown in **Figure 13(A)**. In our experiment, full-α' phase material has only 1.2% elongation and 1877 MPa tensile strength. This smallest elongation and higher tensile strength make fracture surface longer than the other large grains as shown in **Figure 10**. When choosing the grain size of 7.5 μm, the stability of sheared surface length become unstable as shown in **Figure 11**. These characteristics is related to the effect of distribution variation in strain-induced martensitic transformation [26, 27]. If choice the grain size 3.0 μm, the work hardening ability is maintained during micropunching and effect of distribution variation in strain-induced martensitic transformation decrease with the grain size decreasing. Therefore, the deformation and the transformation characteristics are optimized and the stability of sheared surface length is minimized as shown in **Figure 11**. For the stable punching, selecting a grain size 3.0 μm is considered to be effective at the AISI304 micropunching.

5.5 Summary

Fine-grained microstructure in FGSS changes the deformation and phase transformation characteristics in the punching process. In particular, the sheared surface length is more stabilized to improve the punched-out product quality. The punching process can be advanced by using FGSS in practice.

6. Diffusion bonding of FGSS

In the solid-phase diffusion bonding process, the holding temperature (T_H) plays a role to govern the microstructure. When T_H is higher than the recrystallization temperature, the crystal grain easily grows to be coarse one within the bonding time and reduces the strength. Hence, T_H must be lowered as possible to maintain high strength in the mechanical characteristics. In particular, this task in the diffusion bonding of AISI304 must also solve an issue to remove the passive film at low temperature. In the conventional process, T_H becomes higher than 1100 K [28] to eliminate the oxide film on the stainless steel and to accelerate the bonding.

In recent years, new materials have been developed. **Figure 14** shows the newly developed full-martensitic stainless steel (hereafter called WC). This material can accelerate the diffusion bonding at low temperature by introducing a large amount of strain into austenitic stainless steel before bonding. The process of introducing distortion into the material was carried out as follows and as shown in **Figure 14** [29]. First, blocks of AISI304 were cut into 40 × 40 × 20 mm samples (**Figure 15(A)**). The samples were then compressed, cut, and rolled into a 10-mm-thick sheet, so that the equivalent strain in the compression direction was 90% at 573 K (less than

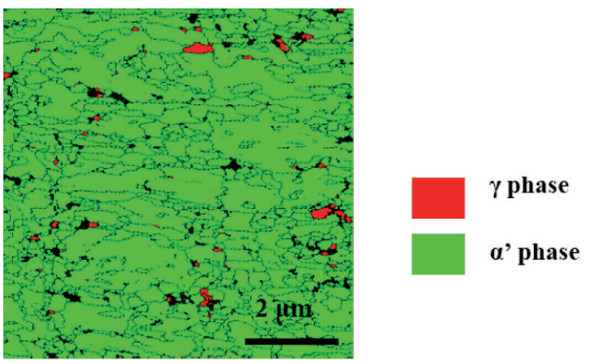

Figure 14.
Developed full-martensitic stainless steel AISI304 (WC).

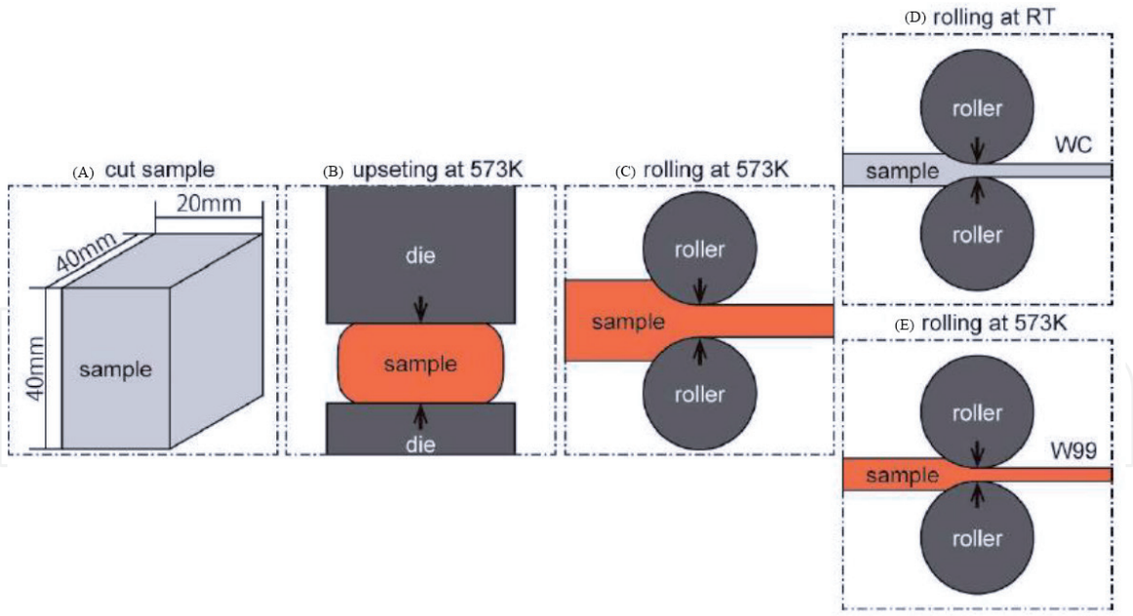

Figure 15.
Schematics of distortion-introduction process. Arrows show compression direction.

the recrystallization temperature) (**Figure 15(B)** and **(C)**). These warm-rolled samples were then rolled to 1-mm thickness at room temperature to transform the microstructure into martensite from austenite (**Figure 15(D)**). To evaluate the effects of the presence or absence of martensite on diffusion bonding, a sample was warm-rolled at 573 K (thus containing deformed austenite) with a reduction of 99% (hereafter called sample W99), as depicted in **Figure 15(E)**. For the cross-tensile test, all the bonding specimens were cut from the 1-mm-thick sheet, and then their bonding areas were mirror polished. The bonding experiment was executed at punching diameter 5 mm and high vacuumed.

Figure 16 shows the effects of strain-induced martensitic and strain for fracture load of bonded AISI304 seats on bonding temperature [30]. WC/WC bonded sample only at 973 K has a fracture load of 2 kN, while T_H must be increased up to 1073 K to attain the same fracture load in case of SOL/SOL bonded sample. That is, WC/WC

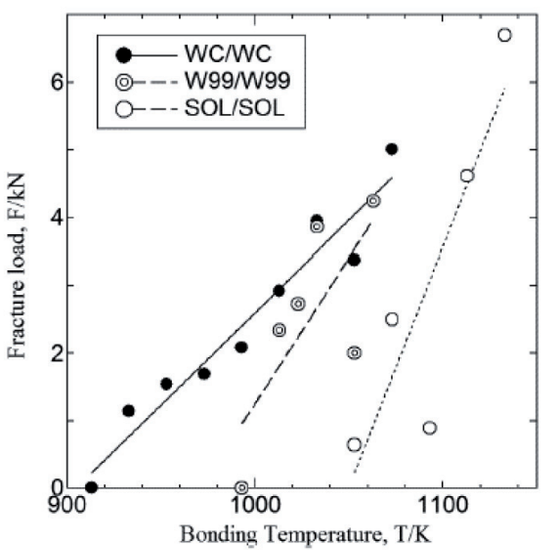

Figure 16.
Effect of strain-induced martensite and strain for fracture load of bonded SUS304 seats on boning temperature.

full-martensitic stainless steel bonding has a capacity to decrease T_H by 100 K against conventional SOL/SOL sample. Furthermore, this T_H for WC/WC bonded sample to attain 2 kN is reduced down to 20,123 K by using the fine-grained W99/W99 boding. This difference in T_H by 50 K between WC/WC and W99/W99 suggests that the martensitic phase works effectively when diffusion bonding stainless steel.

In summary, the holding temperature in diffusion bonding is lowered by using FGSS sheets to successfully fabricate the bonded parts without grain size coarsening. This selection of FGSS sheets for joining is suitable to produce the precision parts with high strength.

7. Surface treatment of FGSS

In standard heat and surface treatments, the stainless steel parts and tools are subjected to high-holding temperature [31]. The first issue of engineering is a crystalline coarsening by the grain growth. As shown in **Figure 17**, FGSS is easy to be coarsened by heat treatment for 1.8 ks at 1073 K [32]. Even below 1000 K, the thermal distortion is issued to deteriorate the microstructure of FGSS; precipitation of carbides and nitrides is also worried to lower the fatigue strength and corrosion toughness. Various nitriding processes were compared to explain how to lower the holding temperature in [33]. The gas nitriding with use of ammonia required for higher temperature than 973 K for industrial surface treatment. The liquid nitriding with use of cyan solutions was applied to surface modification of automotive parts under the temperature of 700–900 K.

Among those nitriding processes, the plasma nitriding has capacity to harden the surface layer in the thickness of 0.1–1 mm without significant loss of corrosion toughness of stainless steels under lower holding temperature. This processing is categorized into two regimes as shown in **Figure 18**; e.g., high-temperature nitriding above 673 K and low-temperature nitriding below 673 K as surveyed in [34] for austenitic stainless steels.

Above the master curves in each stainless steel, the nitrided surface layer is hardened by the fine CrN (chromium nitride) precipitation with large volume fraction [35]. After removal of fragile γ'-Fe_4N precipitated layer (so-called white layer) and diffusion treatment, the nitrided layer with the nitrogen solubility of 0.1–0.2 mass% is utilized as a hardened protective layer of tool-steel and stainless steel parts and dies in commercial [36]. The plasma nitrided AISI316 at "A" just above its master curve in **Figure 18** is mainly hardened by the CrN precipitation. On the other hand, the inner nitriding process at "B" and "C" below the master curve in **Figure 18** is governed by the nitrogen solid solution or the nitrogen

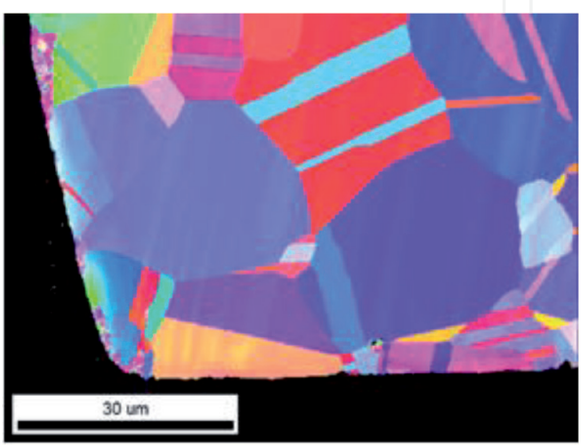

Figure 17.
Grain growth in FGSS by heat treatment for 1.8 ks at 1073 K.

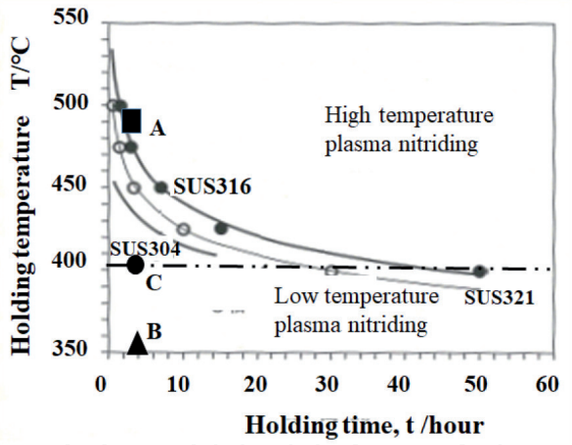

Figure 18.
Relationship of the holding temperature to the holding time in the plasma nitriding.

alloying into AISI316 without formation of nitride precipitates [37]. This low temperature plasma nitriding is proved to be suitable to the surface treatment of FGSS with high hardness and strength and without thermal distortion.

7.1 Plasma nitriding of fine-grained AISI316 at 623 K

The fine-grained AISI316 (FGSS316) specimen was prepared for plasma nitriding at 623 K [38–41]. Its chemical compositions are: [C] = 0.08 mass%, [Si] = 1.00 mass%, [Mn] = 2.00 mass%, [P] < 0.045 mass%, [S] < 0.030 mass%, [Ni] = 12.0 mass%, [Cr] = 17.0 mass%, and [Mo] = 2.5 mass% for iron in balance. The sample surface was mirror polished and cleaned by the ultrasonic cleaner before plasma nitriding. **Figure 19(A)** depicts the high density plasma nitriding system with use of the hollow cathode device to intensify the density of nitrogen ions as well as the NH-radicals. The plasma-processing conditions are also summarized in **Figure 19(B)** in correspondence to "B" in **Figure 18**.

Microstructure and nitrogen mapping on the cross section of this nitrided FGSS316 specimen, describe the average nitrogen diffusion layer from the surface. As shown in **Figure 20(A)**, the nitriding front end locates at the depth of 40 μm from the surface. Although the crystal grain size below this nitriding front end remains the same as before nitriding, these grains are significantly refined in the nitrided layer. The nitrogen mapping in **Figure 20(B)** proves that high nitrogen content uniformly distributes in the nitrided layer from the surface to the depth

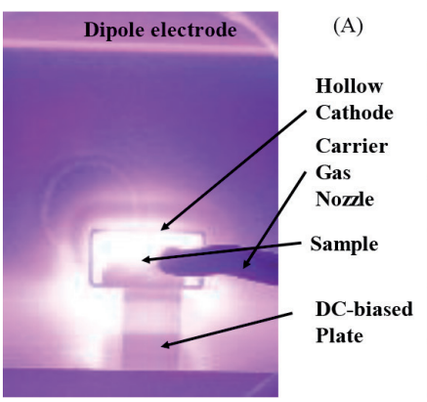

(A)

Item	Parameter
Temperature	623 K
RF-voltage	250 V
DC-bias	-500 V
Pressure	70 Pa
Carrier gas	N_2-H_2 mixture
Device	Hollow cathode

(B)

Figure 19.
High density plasma nitriding system with use of the hollow cathode for low temperature plasma nitriding of FGSS316. (A) Schematic view of nitriding system, and (B) plasma nitriding conditions in the following experiments.

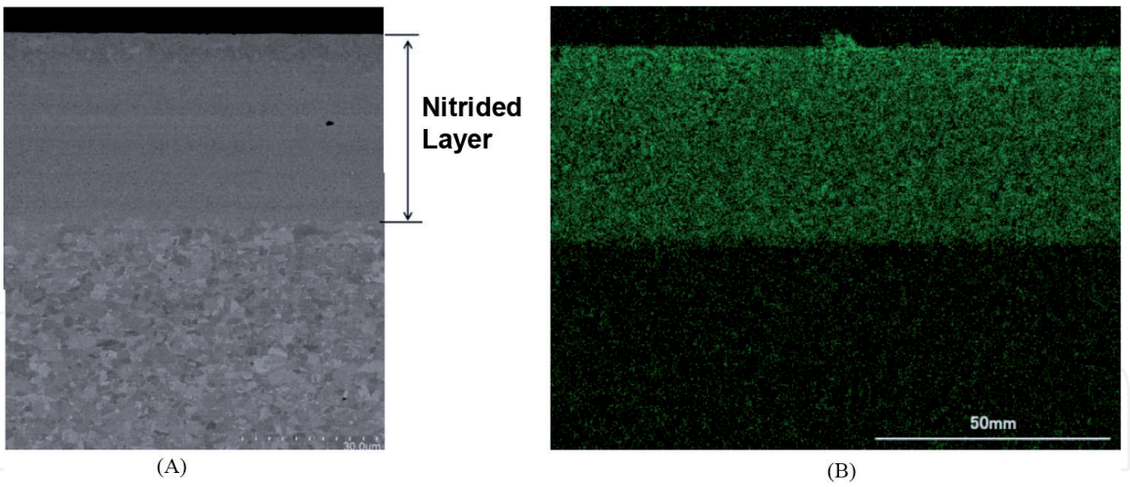

Figure 20.
Cross-sectional image of the plasma nitrided FGSS316 for 14.4 ks at 623 K. (A) SEM image and (B) nitrogen mapping analyzed by EDX.

of 40 μm. This implies that the thick nitrided layer with high nitrogen content and refined grains is formed by the present surface treatment at 623 K.

Figure 21 compares the XRD diagrams of FGSS316 specimen surfaces before and after plasma nitriding at 623 K for 14.4 ks. XRD diagram of bare FGSS316 is characterized by γ (111)-peak at $2\theta = 43.5^{\circ}$ as well as γ (200)-peak at $2\theta = 50.7^{\circ}$, respectively. After nitriding, this γ (111)-peak shifts from 43.5° to 40.5°, and, γ (200)-peak, from 50.7° to 46.6°, respectively. A new peak detected at $2\theta = 43.65^{\circ}$ is identified as α' (110). Besides for these three peaks, no other peaks are detected even by the narrow scanned XRD in **Figure 21**; no chromium and iron nitrides are synthesized in this plasma nitriding. Nitrogen solute atoms do not react with the constituent atoms such as iron and chromium in FGSS316 but work as a constituent alloying element in the γ-lattice of FGSS316. The nitrogen solute atoms occupy the octahedral vacancy sites in the γ-lattices in FGSS316. This in situ nitrogen solute occupation with vacancy sites in the γ-lattices accompanies with the γ-lattice expansion in elasticity in **Figure 21**, and, characterizes the nitrogen supersaturation process in the low-temperature nitriding.

Difference in the holding temperature between "A" and "B/C" in **Figure 18** reflects on the inner nitriding mechanism. High-temperature nitriding is driven by the nitrogen body-diffusion process with the precipitation reaction of diffusing nitrogen atom and constituent elements in FGSS316 to nitrides. Low-temperature nitriding is controlled by the nitrogen boundary-diffusion with the nitrogen

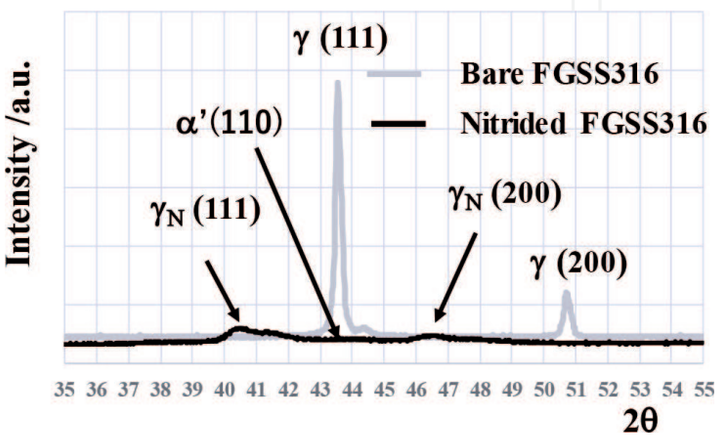

Figure 21.
XRD diagram of FGSS316 specimens before and after plasma nitriding at 623 K for 14.4 ks.

supersaturation in concurrent. This difference reflects on the microstructure evolution during the inner nitriding. Let us analyze this by using EBSD.

Figure 22(A) depicts the phase mapping on the cross section of nitrided FGSS316 at 623 K. The original microstructure below the nitriding front end has mainly austenitic phase but partially includes the martensitic phase. This phase transformation is strain-induced from the original γ-phase by intense rolling during fabrication of FGSS316 plates. Total volume fraction of α'-phase is only 6%. This implies that highly strained γ-phase grains must be massively transformed into α'-phase and that most of γ-phase remains as a matrix. On the other hand, this martensitic phase distributes finely together with γ-phase above the nitriding front end. The volume fraction of this α'-phase reaches to 70%. This implies that the nitrided layer has fine γ-α' two-phase structure. The original matrix structure, seen below the nitriding front end in **Figure 22(A)**, disappears and turns to be fine two-phase structure with nitrogen supersaturation.

As before mentioned, this nitrogen supersaturation accompanies with the plastic straining as well as the γ to α' phase transformation by elastic straining in the above. **Figure 22(B)** shows the KAM distribution on the same cross section. Besides for the upper part with remaining relatively large γ-phase regions in **Figure 22(A)**, the two-phase structured grains in the nitrided layer have high-angled misorientation; almost every grain in the nitrided layer is plastically strained. As explained by **Figure 21**, the nitrogen supersaturated zones in each grain are forced to expand themselves in elasticity; while unsaturated zones have no elastic strains. Considering that strain incompatibility might be induced between these nitrogen-saturated and unsaturated zones in every nitrided grain, the unsaturated zones are plastically strained. KAM distribution in **Figure 22(B)** represents the equivalent plastic strain distribution by this plastic straining.

Figure 22(C) shows the inverse pole figure in the nitrided layer. The original FGSS matrix, seen above the nitriding front end, turns to have much refined microstructure. The grain size is measured to be less than 100 nm or the spatial resolution limit of EBSD. This grain-size refinement is driven by intense plastic straining as seen in **Figure 22(B)**.

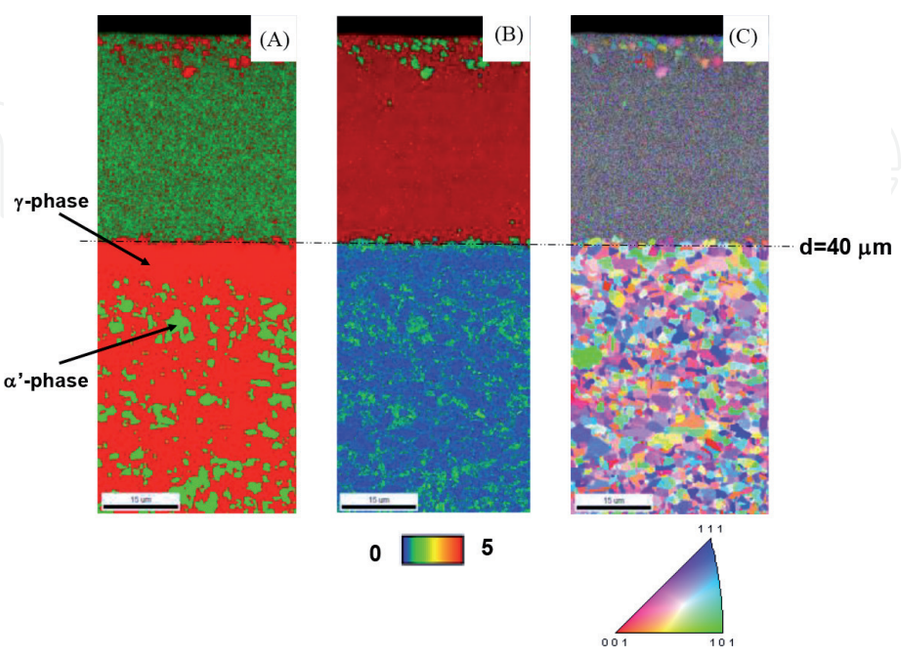

Figure 22.
Microstructure on the cross section of nitrided FGSS316 at 623 K for 14.4 ks. (A) Phase mapping, (B) KAM distribution, and (C) inverse pole figures.

7.2 In situ two-phase structuring and refinement

This in situ formation of two-phase microstructure with refined grains in **Figure 22** is suitable to industrial applications. Different from the coarse mixture of γ-phase and α'-phase grains in normal two-phase stainless steels [42], this fine γ-α' microstructure results in high hardness and toughness. In addition, high nitrogen solute concentration improves the corrosion toughness even in severe conditions. Let us evaluate on these features by hardness testing and nitrogen depth profile measurement.

Figure 23(A) depicts the hardness depth profile of nitrided FGSS316 at 623 K. Hardness in the nitrided layer with the thickness of 40 μm is uniform by 1400 HV, and, gradually decreases down to the matrix hardness across the nitriding front end. The grain-size refinement in **Figure 22** contributes to this high hardness. As reported in [31, 33, 35], the maximum surface hardness by the high temperature plasma nitriding above 750 K was often limited by 1200–1300 HV. That hardness monotonously decreased with the depth except for high chromium alloys [31, 35]. Hence, the fact that nitrided layer is uniformly hardened layer by 1400 HV in average even without nitride precipitation, is a new knowledge to surface treatment of stainless steels and tool steels. As also stated in [31, 33, 35, 43], the maximum nitrogen solubility except for the bound nitrogen atoms in nitrides is limited by 0.1–0.2 mass%. Most of chromium solutes are reacted with diffusing nitrogen atoms and bound into CrN in the nitrided stainless steels over 750 K; those nitrided steels reduce their original corrosion toughness [44]. **Figure 23(B)** shows the nitrogen solute content depth profile. The surface nitrogen content becomes higher than 6 mass%, and, this [N] is nearly constant by 4–5 mass% down to the nitriding front end. As had been studied in [43, 45], this high nitrogen solute content significantly promotes the corrosion toughness even under the dipping condition into HCl solutions. This improvement of mechanical and electro-chemical properties by the plasma nitriding is attractive to industrial applications.

7.3 Plasma nitrided FGSS316 dies at 673 K

This low temperature plasma nitriding was first applied to fabricate the FGSS316 punch for microembossing the regular-square meshing pattern with the line width of 50 μm and pitch of 250 μm into aluminum plate. In the conventional die-fabrication, this textured multi-head punch is made by drilling each regular-square microcavity with the edge of 200 μm. The number of microcavities reaches to 3200 on the punch with the size of 20 × 10 mm. When using the milling tool with the diameter of 10 μm and machining a single microcavity by the speed of 50 μm/s, including the cutting path changing time, and the threading depth of 10 μm, the

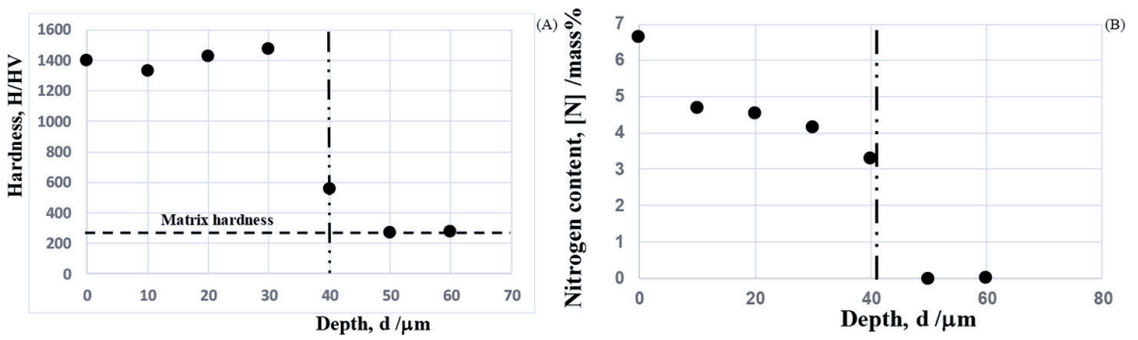

Figure 23.
Hardness and nitrogen solute content depth profiles of nitrided FGSS316 at 623 K. (A) Hardness and (B) nitrogen solute content.

total machining time is estimated to be 1, 280 ks, or 356 h. This micromachining provides no solution to fabrication of the multi-arrayed punch with regular-square meshing heads. After [46, 47], the plasma printing method with use of the low temperature plasma nitriding provides a solution to fabricate this die as shown in **Figure 24**. A meshing pattern is first printed by using the screen with a unit pattern in **Figure 24(A)**. The unprinted cross-meshing surfaces are selectively nitrided at 673 K for 14.4 ks ("C" in **Figure 18**) in **Figure 24(B)**. After sand-blasting, this unit pattern transforms to **Figure 24(C)**. The microtexture arrayed punch is fabricated as shown in **Figure 24(D)** to have regular meshing texture in **Figure 24(E)**.

The takt time of this processing is only 18 ks, 70 times shorter than micromilling even excluding the cutting tool life as well as the preparation for CAM data before actual machining.

7.4 Plasma nitrided FGSS316 wires at 623 K

FGSS316 wire is expected to be working as a tension member and component for reinforcement of prestressed concrete and for steel wires in medical equipment. These members often experience the friction and wear in severe surface chemical conditions; they have to be surface treated to improve their wear resistance and corrosion toughness. The low temperature plasma nitriding at 623 K is also effective to improve the surface hardness as well as the electro-chemical properties. FGSS316 wire with the diameter of 2.6 mm was prepared for plasma nitriding at 623 K for 14.4 ks by 70 Pa.

Figure 25 depicts the SEM image and nitrogen mapping on the cross section of FGSS316 wire. The wire surface is homogeneously processed to form the nitrided layer with high nitrogen concentration. The layer thickness approaches to 35 μm, which is a bit less than that seen in **Figures 22** and **23** for nitrided FGSS316 plates. A hard wire often experiences the bending and wiping as well as the tensile stretching in its usual operation. Owing to the surface hardening of wire by the plasma nitriding at 623 K, the bending and torsion rigidities as well as the tensile rigidity are expected to increase [48].

7.5 Summary

The plasma nitriding in the lower temperature regime than 700 K provides a means to modify the microstructure of FGSS by nitrogen alloying and to

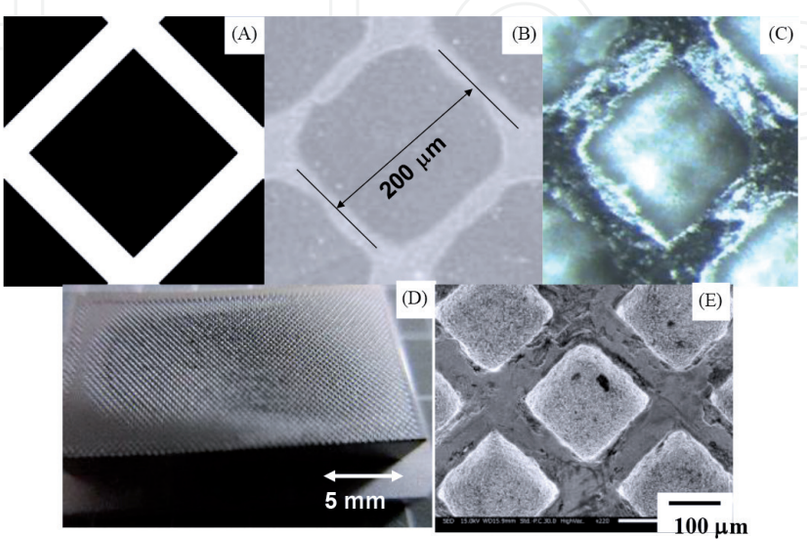

Figure 24.
Efficient production of the multi-head punch by the plasma nitriding with use of the plasma nitriding at 673 K. (A) Meshing pattern on the screen, (B) plasma nitrided pattern on the FGSS316 die, (C) three dimensionally textured FGSS316, (D) microtextured FGSS316 punch, and (E) meshing-texture arrayed punch.

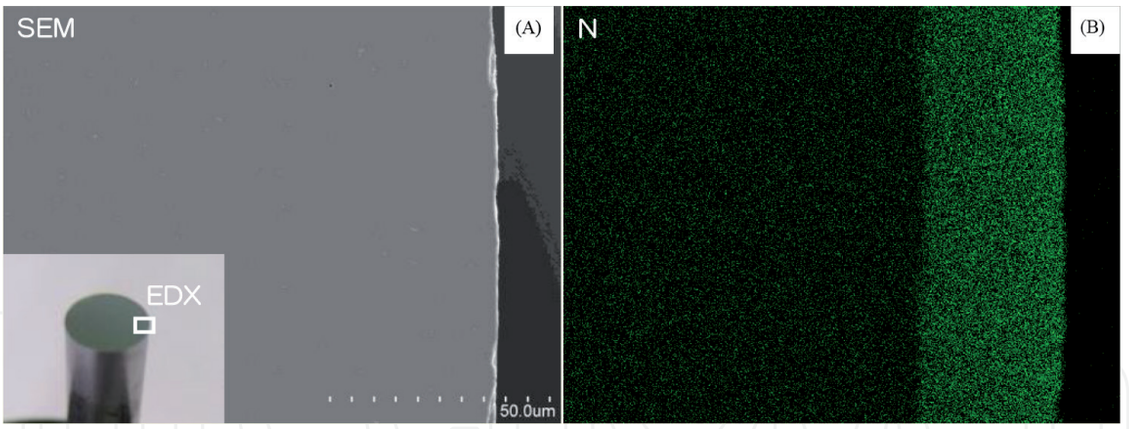

Figure 25.
Plasma nitrided FGSS316 wire at 623 K for 14.4 ks. (A) Cross-sectional SEM image, and (B) nitrogen mapping on the cross section.

significantly improve the mechanical and electro-chemical properties of FGSS. The nitrided FGSS316 layer consists of homogeneous two-phase microstructure with finer grain size than 0.1 μm. Since the original grain size of FGSS316 is 1.7 μm, the strength of nitrided FGSS316 increases by more than 10 times after the Hall-Petch relationship. This surface treatment by low temperature plasma nitriding is available not only in improvement of the wear resistance of dies for microstamping and forging but also in high strengthening of wires for medical equipment. In the former, the micropunch with multi punch head array is fabricated by blasting the un-nitrided substrate surface areas. This plasma printing is responsible to make microtextured die and punch in much less takt time for microembossing and micropiercing the metallic and polymer sheets. In the latter, the stainless steel bars, wires and fibers are surface treated to have higher nitrogen content layer. This nitrogen supersaturated surface layer works as a hardened and strengthened layer even after warm and hot drawing them to smaller diameters. Effect of supersaturated nitrogen distribution in them on their strength and ductility could be of much importance in application to industries and medicals.

8. Conclusion

Fine-grained stainless steels (FGSS) have grown up as a key material for mechanical and short-pulse laser machining, for metal forming and diffusion bonding, and for surface treatment to fabricate the miniature automotive parts and fine medical components. Their high strength without loss of ductility by grain-size refinement is not only attractive to improve the work and die material performance but also effective to enhance the workability in their integrated manufacturing. Smooth finish in mechanical machining as well as deep cutting by laser machining are intrinsic to FGSS. Precise shaping by micropiercing as well as low temperature diffusion bonding are also unique to FGSS. In their plasma nitriding, the holding temperature is significantly lowered down to 623 K for homogeneous formation of the hardened layer by 1400 HV with the thickness of 40 μm. Each advancement in this integrated manufacturing is fused and edited to construct the production line toward FGSS-based fine medical tools and precise mechanical parts. In particular, FGSS bars, wires, sheets, and plates transform to high strength, precisely shaped reliable media in mechanical units and medical equipments.

Acknowledgements

The authors would like to express their gratitude to Prof. S. Torizuka (Hyogo Prefectural University), Mr. E. Muramatsu, Mr. Y. Suzuki, and Mr. T. Yoshino (KSJ) for their help in experiments.

Conflict of interest

The authors declare no conflict of interest.

Author details

Tatsuhiko Aizawa[1*], Tomomi Shiratori[2] and Takafumi Komatsu[2]

1 Surface Engineering Design Laboratory, SIT, Tokyo, Japan

2 Komatsu-Seiki Kosakusho, Co. Ltd., Suwa, Japan

*Address all correspondence to: taizawa@sic.shibaura-it.ac.jp; shira@eng.u-toyama.ac.jp

References

[1] Hall EO. The deformation and ageing of mild steel: III discussion of results. Proceedings of the Physical Society. Section B. 1951;**64**(9):747

[2] Petch NJ. The cleavage strength of polycrystals. Journal of the Iron and Steel Institute. 1953;**174**:25-28

[3] Sakai G, Horita Z, Langdon TG. Grain refinement and superplasticity in an aluminum alloy processed by high-pressure torsion. Materials Science and Engineering: A. 2005;**393**(1-2):344-351

[4] Zhilyaev AP, Oh-Ishi K, Langdon TG, McNelley TR. Microstructural evolution in commercial purity aluminum during high-pressure torsion. Materials Science and Engineering A. 2005;**410**:277-280

[5] Torizuka S, Umezawa O, Tsuzaki K, Nagai K. Shape, size and crystallographic orientation of the ferrite grains formed at grain boundaries of deformed austenite in a low carbon steel. Tetsu to Hagane. 2000;**86**(12):807-814

[6] Tomimura K, Takaki S, Tokunaga Y. Reversion mechanism from deformation induced martensite to austenite in metastable austenitic stainless steels. ISIJ International. 1991;**31**(12):1431-1437

[7] Murata Y, Ohashi S, Uematsu Y. Recent trends in high strength stainless steel. Tetsu to Hagane. 1992;**78**(3):346-353

[8] Simoneau A, Ng E, Elbestawi MA. Chip formation during microscale cutting of a medium carbon steel. International Journal of Machine Tools and Manufacture. 2006;**46**(5):467-481

[9] Lee WB, Cheung CF, To S. Materials induced vibration in ultra-precision machining. Journal of Materials Processing Technology. 1999;**19**(89):318-325

[10] Lee WB. Prediction of microcutting force variation in ultra-precision machining. Precision Engineering. 1990;**12**(1):25-28

[11] Lee WB, Cheung CF, To S. A microplasticity analysis of micro-cutting force variation in ultra-precision diamond turning. Journal of Manufacturing Science and Engineering. 2002;**124**(2):170-177

[12] Furukawa Y, Moronuki N. Effect of material properties on ultra-precise cutting processes. CIRP Annals. 1988;**37**(1):113-116

[13] Komatsu T, Matsumura T, Torizuka S. Effect of grain size in stainless steel on cutting performance in micro-scale cutting. International Journal of Automation Technology. 2011;**5**(3):334-341

[14] Komatsu T, Yoshino T, Matsumura T, Torizuka S. Effect of crystal grain size in stainless steel on cutting process in micromilling. Procedia CIRP. 2012;**1**:150-155

[15] Komatsu T, Musha Y, Yoshino T, Matsumura T. Surface finish and affected layer in milling of fine crystal grained stainless steel. Journal of Manufacturing Processes. 2015;**1**(19):148-154

[16] Fujita M, Hashida M. Femtosecond-laser processing. Journal of Plasma and Fusion Research. 2005;**81**:195-201

[17] Siegel F, Klug U, Kling R, Ostendorf A. Extensive micro-structuring of metals using picosecond pulses—Ablation behavior and industrial relevance. Journal of Laser Micro/Nanoengineering. 2009;**4**(2):104-110

[18] Komatsu T. Effects of grain size on the groove depths in microlaser cutting of austenitic stainless steel SUS304. International Journal of Automotive Technology. 2015;**9**(6):636-645

[19] Vollertsen F, Biermann D, Hansen HN, Jawahir IS, Kuzman K. Size effects in manufacturing of metallic components. CIRP Annals—Manufacturing Technology. 2009;**58**:566-587

[20] Engel U, Eckstein R. Microforming—From basic research to its realization. Journal of Materials Processing Technology. 2002;**125-126**:35-44

[21] Kals TA, Eckstein R. Miniaturization in sheet metal working. Journal of Materials Processing Technology. 2000;**103**:95-101

[22] Shrinivas V, Varma SK, Murr LE. Deformation-induced martensitic characteristics in 304 and 316 stainless steels during room temperature rolling. Metallurgical and Materials Transactions A. 1995;**26**:661-671

[23] Tamura I. On the TRIP steel. Tetsu to Hagane. 1970;**56**:429-445

[24] Shiratori T, Suzuki Y, Nakano S, Yang M, Komatsu T. Effects of grain size on the sheared surface in micropiercing of austenitic stainless steel SUS304. Manufacturing Review. 2015;**2**:9

[25] Nomura K, Kubushiro K, Sakakibara Y, Takahashi S, Yoshizawa H. Effect of grain size on plastic strain analysis by EBSD for austenitic stainless steels with tensile strain at 650°C. Journal of the Society of Materials Science, Japan. 2012;**61**:371-376

[26] Shiratori T, Katoh M, Sato N, Yoshino T, Nakano S, Yang M. Deformation and transformation behavior in micropiercing of fine-grained SUS304. Journal of the Japan Society for Technology of Plasticity. 2017;**58**:936-942

[27] Shiratori T, Yoshino T, Suzuki Y, Katoh M, Nakano S, Yang M. Deformation and transformation behavior in micropiercing of SUS304. Procedia Manufacturing. 2018;**15**:1452-1458

[28] Ohashi O, Suga S. Effect of surface composition on diffusion welding in stainless steel. Journal of the Japan Institute of Metals. 1992;**56**:579-585

[29] Sato N, Yoshino T, Shiratori T, Nakano S, Katoh M. Accelerative effects of diffusion bonding on recrystallization with reversion of deformation-induced martensite in SUS304. ISIJ International. 2016;**56**:1825-1830

[30] Katoh M, Sato N, Shiratori T, Suzuki Y. Reduction of diffusion bonding temperature with recrystallization at austenitic stainless steel. Tetsu to Hagane. 2016;**102**:34-39

[31] Kuwahara H. Surface treatment of iron base alloys by plasma technology [PhD thesis]. Kyoto University; 1992

[32] Aizawa T, Saitoh T, Shiratori T. Micro-joining of shaped stainless steel sheets for fuel injection orifice with high misting capability. In: Proc. 22nd Metal Forming (ESAFORM2019); 8-10, May 2019

[33] Anzai M, editor. Heat and Surface Treatment of Die Materials. Tokyo, Japan: Nikkan-Kogyo-Shinbunsha; 2011

[34] Aizawa T. Characterization on the properties of nitrided layer in dies and molds: Low temperature plasma nitrided stainless steels. Bulletin of the JSTP. 2019;**2**(19):411-415

[35] Granito N, Kuwahara H, Aizawa T. Normal and anormal

microstructure of plasma nitrided Fe-Cr alloys. Journal of Materials Science. 2002;**37**(4):835-844

[36] Aizawa T, Sugita Y. High density RF-DC plasma nitriding of steels for die and mold technologies. Research Report. SIT. 2013;**57**(1):1-10

[37] Imai Y, Murata T, Sakamoto M. High Nitrogen Steels. Tokyo: Agune; 2005

[38] Aizawa T, Yoshihara S-I. Homogeneous and heterogeneous micro-structuring of austenitic stainless steels by the low temperature plasma nitriding. IOP Conference Series: Materials Science and Engineering. 2018;**372**:012049-1-012049-6

[39] Aizawa T. Chapter 3—Low temperature plasma nitriding of austenitic stainless steels. In: Stainless Steels. Rijeka: IntechOpen; 2019. pp. 31-50

[40] Aizawa T, Yoshihara S-I. Inner nitriding behavior and mechanism in stainless steels type AISI316 at 623 K. In: Proc. 13th SEATUC Conf. 2019. pp. 123-128. OS07

[41] Aizawa T, Yoshino T, Shiratori T, Yoshihara S-I. Grain size effect on the nitrogen super-saturation process into AISI316 at 623 K. ISIJ International. 2019;**69**:1-7

[42] Hiraoka Y, Inoue K. Prediction of nitrogen distribution in steels after plasma nitriding. Denki-Seiko. 2010;**86**:15-24

[43] Aizawa T. Functionalization of stainless steels via low temperature plasma nitriding. In: Proceedings of the 7th Annual Basic Science International Conference; Malang, Indonesia; 2017. pp. 1-16

[44] Aizawa T, Yoshihara S-I. Inner nitriding behavior and mechanism in stainless steels at 753 K and 623 K. SJSE. 1; 2019 (in press)

[45] Aizawa T, Yoshihara S-I. Microtexturing into AISI420 dies for fine piercing of micropatterns into metallic sheets. Journal of the Japan Society for Technology of Plasticity. 2019;**60**:53-57

[46] Shiratori T, Aizawa T, Saito Y, Wasa K. Plasma printing of AISI316 multi-punch die micro-embossing into copper plates. Metals—Open Access Metallurgy Journal. 2019;**9**(4):396/1-396/11

[47] Aizawa T, Shiratori T, Wasa K. Plasma-printed AISI316L multi-punch array for fabrication of aluminum heatsink with micro-pillar fins. In: Proc. 3rd WCMNM. 2019. pp. 220-223

[48] Aizawa T, Shiratori T, Yoshino T, Suzuki Y, Kamotsu T. Microstructure evolution of fine grained AISI316 wire plasma nitrided at 623 K through uniaxial tensile loading. ISIJ International; 2019. (in press)